Waveguide-Coupled Colloidal Quantum Dot Light Emitting Diodes and Detectors on a Silicon Nitride Platform

Lukas Elsinger, Robin Petit, Frederik Van Acker, Natalia K. Zawacka, Ivo Tanghe, Kristiaan Neyts, Christophe Detavernier, Pieter Geiregat, Zeger Hens, and Dries Van Thourhout*

Colloidal quantum dots (QDs) are an attractive light source for visible photonics, in particular their widely tunable emission wavelength, inexpensive wet-chemical synthesis and straight-forward hybrid integration can make the difference. In this work, integrated light-emitting diodes are demonstrated based on CdSe/CdS QDs, with the emission directly coupled to a silicon nitride waveguide. The devices feature a record current density of up to 100 A cm^{-2} and a maximum on-chip power density of almost 1.5 W cm^{-2} in a single-mode waveguide. Operated as detectors, the photodiodes have a low dark current of 1.5 µA cm^{-2}. It is anticipated, that the devices will find an application in chip-based absorption spectroscopy and bio-sensing, as they can be post-processed on foundry-fabricated waveguide platforms, at a low cost. In addition, this approach provides the missing low-loss waveguide layer, necessary for building an electrically pumped laser using colloidal QDs.

Dr. L. Elsinger, I. Tanghe, Prof. D. Van Thourhout
Photonics Research Group and Center for Nano- and Biophotonics
Ghent University - imec
Technologiepark 126, Gent 9052, Belgium
E-mail: Dries.VanThourhout@UGent.be

R. Petit
Conformal Coating of Nanomaterials Group, LumiLab and Center for Nano- and Biophotonics
Ghent University
Krijgslaan 281-S1, Gent 9000, Belgium

Prof. C. Detavernier
Conformal Coating of Nanomaterials Group and Center for Nano- and Biophotonics
Ghent University
Krijgslaan 281-S1, Gent 9000, Belgium

F. Van Acker, Prof. K. Neyts
Liquid Crystals and Photonics Group and Center for Nano- and Biophotonics
Ghent University
Technologiepark 126, Gent 9052, Belgium

N. K. Zawacka, Prof. P. Geiregat, Prof. Z. Hens
Physics and Chemistry of Nanostructures and Center for Nano- and Biophotonics
Ghent University
Krijgslaan 281-S3, Gent 9000, Belgium

1. Introduction

Colloidal semiconductor nanocrystals or QDs are appealing gain materials for optical amplifiers and lasers. Especially in the case of optically pumped lasers, multiple studies have demonstrated the combined advantages of a tunable emission spectrum, high material gain, and suitability for solution-based processing.[1–3] In addition, reliable approaches to fabricate QD-based microlasers have been established[4,5] and pathways identified to shift from femtosecond pulsed excitation to continuous-wave optical pumping,[6,7] at power levels around 10 kW cm^{-2}, compatible with cheap blue laser diodes. The demonstration of electrically pumped QD lasers, on the other hand, still remains a challenge. Building on the progress in colloidal QD light emitting diodes[8] (QD-LEDs), optical gain has been achieved with DC electrical pumping, by implementing a current focusing approach.[9] However, to attain lasing operation, LED designs that support the high current densities required to sustain population inversion must be integrated with a low-loss cavity. One approach to address this is to use index confinement in the active material, combined with a patterned charge transport layer providing distributed feedback.[10] However, in such a device a sufficiently thick QD film is needed to support a confined optical mode. For thin QD layers, which can be inverted with the available current density, increasing passive optical losses strongly compromise lasing operation. As an alternative, we propose a novel design with a QD-LED structure in the evanescent field of a guided optical mode, allowing to significantly reduce passive optical losses for thin QD layers and enabling multiple means of optical feedback.

In this work, we demonstrate a waveguide-coupled QD-LED, the basic building block for future laser designs. We therefore combined an adapted CdSe/CdS QD-LED structure with silicon nitride (SiN) integrated photonics. SiN recently emerged as a versatile platform for on-chip visible and infrared photonics, with applications in bio-sensing and spectroscopy.[11] While SiN enables high performance passive components with propagation losses as low as 1 dB m^{-1},[12] the heterogeneous integration of active components is essential for advanced functionality. For example, fast Pockels modulators[13] and III-V amplifiers and lasers[14,15] have been integrated on silicon nitride, as well as

ADVANCED
SCIENCE NEWS

www.advancedsciencenews.com
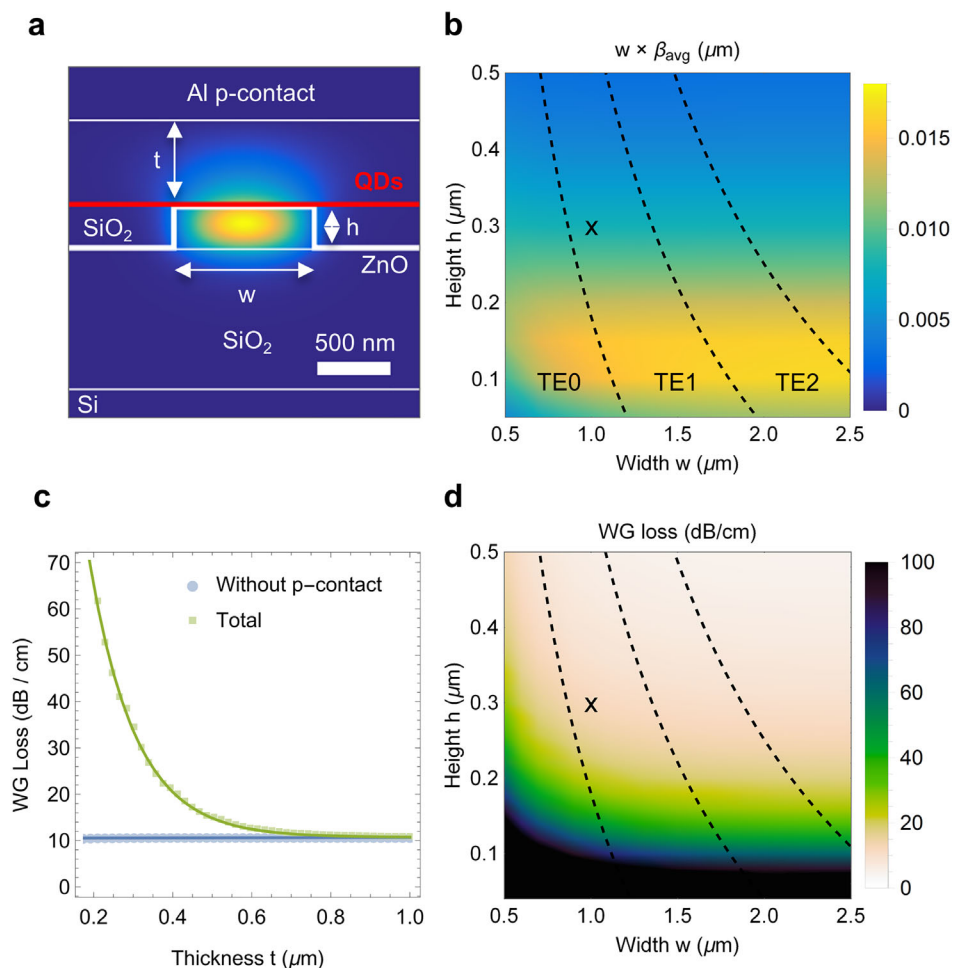
www.lpr-journal.org

LASER
& PHOTONICS
REVIEWS

Figure 1. Simulation results of coupling efficiency and waveguide loss for different geometries. a) Mode profile of the fundamental TE mode for the fabricated geometry and a simulation wavelength of 650 nm. b) Figure of merit for the power coupled to the fundamental TE mode, for a given organics thickness of $t = 600$ nm. c) Waveguide loss originating from the p-contact metal for a given width ($w = 1$ µm) and height ($h = 300$ nm) of the silicon nitride. d) Dependence of the passive waveguide loss on the geometry, for a given organics thickness of $t = 600$ nm. First-order interpolation of the simulation results was used for the display in (b) and (d), the dashed lines represent the onset of higher order modes for the simulation wavelength.

optically-pumped QD lasers.[4] To extend this work to integrated QD-LEDs, we started from an efficient so-called inverted QD-LED stack,[8,16] consisting of a QD film in-between organic materials for hole injection and ZnO nanocrystals for electron injection. However, straightforward integration of this stack on top of a SiN waveguide would induce prohibitive propagation losses of several dB µm^{-1}. A key to overcoming this issue, was developing a low-loss ZnO n-contact layer. In combination with the inherent current focusing architecture of our waveguide-coupled QD-LEDs, this enabled a record current density of 100 A cm^{-2}, while minimizing passive losses. Furthermore, the presented devices can also be operated as integrated photodiodes, making them a versatile building block to functionalize SiN integrated photonics. At the same time, our work constitutes a major step on the way to an electrically pumped QD laser.

2. Device Design

Figure 1a shows the device cross-section, with an overlay of the fundamental transverse electric (TE) waveguide mode profile.

The silicon nitride waveguide with width w and height h is overcoated with a 10 nm thin ZnO n-contact layer. Silicon oxide acts as a side-cladding of the waveguide, enabling the uniform deposition of a ≈20 nm colloidal CdSe/CdS quantum dot layer. The QDs with a core/shell diameter of 3.7/7.5 nm were optimized for a high intrinsic gain and a low threshold.[17] Organic hole transport layers with a total thickness t and an aluminum p-contact complete the device. To optimize the geometry and find a suitable trade-off between coupling efficiency and propagation loss, we performed finite element (FE) and finite difference time domain (FDTD) simulations with a commercial software package (Lumerical). The colloidal CdSe/CdS QDs can be approximated as isotropic dipole emitters, due to their random orientation in the device.[18] However, only one dipole orientation couples efficiently to the fundamental TE waveguide mode. The average coupling efficiency β_{avg}, for quantum dots on top of the waveguide has a maximum for narrow single-mode waveguides, due to higher mode overlap compared to wider multi-mode waveguides. Yet, this does not mean that single-mode waveguides will perform better, since there will be more electrically contacted

**ADVANCED
SCIENCE NEWS**

www.advancedsciencenews.com

**LASER
& PHOTONICS
REVIEWS**

www.lpr-journal.org

Table 1. Estimated waveguide loss contributions for the fundamental TE mode with the fabricated dimensions, assuming QD absorption in absence of electrical or optical pumping.

Wavelength [nm]	610 (band-edge)	642 (EL peak)	650
SiN (dB cm^{-1})	≤ 1	≤ 1	≤ 1
ZnO (dB cm^{-1})	9	9	9
Al p-contact (dB cm^{-1})	1	2	2
QDs (dB cm^{-1})	405	44	14
Total (dB cm^{-1})	≤ 416	≤ 56	≤ 26

emitters on top of a wider waveguide. A more meaningful figure of merit is $w \times \beta_{avg}$, which is proportional to the total spontaneous emission coupled to the fundamental TE mode. Results for different geometries are displayed in Figure 1b, using a first-order interpolation between simulated values. The dashed black lines mark the onset of higher order TE modes for the simulation wavelength of 650 nm. It can be seen, that the coupled spontaneous emission depends weakly on the width and reaches a maximum for a height between 100 and 150 nm. For wider multi-mode waveguides, part of the spontaneous emission is coupled to the higher-order modes. However, for integrated photonics applications single-mode devices are preferred, to avoid spurious effects originating from mode mixing. All simulations were performed with refractive index values of the organic layers, ZnO and silicon nitride extracted from ellipsometry measurements. To accurately determine the loss of the optimized ZnO layer, we performed cut-back measurements, extracting an imaginary refractive index of $k = 2.5 \times 10^{-4}$ (see Section S4, Supporting Information). Figure 1c visualizes the influence of the p-contact metal on the waveguide loss, for fixed dimensions of the silicon nitride waveguide ($w = 1\,\mu m$, $h = 300\,nm$) and assuming loss-less organic layers. The metal loss component shows the expected dependence on the overlap with the evanescent field, resulting in an exponential decay of the loss with the thickness t. Only for a sufficient separation, determined by the thickness of the organic layers, reasonable loss can be achieved. For example, for an organic layer thickness of $t = 500\,nm$, simulations predict a metal loss of 4 dB cm^{-1}, which was confirmed by cut-back measurements (see Section S5, Supporting Information). Since there are also electrical and fabrication constraints for the maximum thickness of the organic layer, we fixed the parameter at $t = 600\,nm$. This corresponds to a simulated excess loss of 2 dB cm^{-1} due to the aluminum layer for $w = 1\,\mu m$ and $h = 300\,nm$. Figure 1d shows the dependence of the total waveguide loss on the width and height of the silicon nitride, for an organics thickness of $t = 600\,nm$. Clearly, thin silicon nitride waveguides give rise to increasing losses, due to the larger mode overlap with the ZnO layer and the p-contact metal. A height of 300 nm provides a good trade-off between loss and coupling efficiency. Also, narrower single-mode waveguides show higher passive losses due to a larger mode overlap with the ZnO layer on the waveguide sidewalls and the quantum dots next to the waveguide, which were included in the simulation of passive losses, since they will only cause absorption. **Table 1** summarizes the different loss contributions for the fundamental TE mode with the fabricated dimensions, including QDs on top of the waveguide as reported

below. Transverse magnetic (TM) waveguide modes are strongly suppressed in the design, due to their larger overlap with the aluminum p-contact layer, resulting in simulated passive waveguide losses exceeding 180 dB cm^{-1} (see Section S6, Supporting Information).

3. Fabrication

Based on the simulation results we targeted dimensions of $w = 1\,\mu m$, $h = 300\,nm$, and $t = 600\,nm$ for the fabrication. To ease the prototyping, the results presented here use waveguides fabricated using e-beam lithography. But it would also be possible to do the following post-processing steps (see **Figure 2**a–e) on waveguides processed by a foundry, since 300 nm is a commonly available standard thickness for silicon nitride.[19]

Silicon nitride waveguides were fabricated on silicon samples with a 1 µm thermal oxide layer, on which a 300 nm silicon nitride layer was deposited by plasma enhanced chemical vapor deposition (PECVD). To pattern the waveguide layer, we used electron-beam lithography with a positive resist (ARP-6200, Allresist) and reactive ion etching (RIE) in CF$_4$ and H$_2$ chemistry. Unlike common inverted LED designs found in literature,[16] we do not use a combination of a transparent conductive oxide and ZnO nanocrystals for electron injection. Instead, we employed atomic layer deposition (ALD) to conformally coat the waveguides with a 10 nm thin layer of polycrystalline ZnO, serving as an electron transport and injection layer. Subsequently, we deposited a 15 nm Al$_2$O$_3$ ALD layer, acting as passivation and etch-stop layer, followed by a short annealing step, reaching a maximum of 400 °C in N$_2$ and H$_2$ atmosphere. This procedure resulted in a high-performance ZnO layer, with a favorable trade-off between conductivity (sheet resistance of 1.2 ±0.1 kΩsq^{-1}) and optical losses (see Section 4, Supporting Information). After locally removing the Al$_2$O$_3$ in dilute KOH, metal contacts (20 nm Ti/100 nm Au/20 nm Ti) were patterned next to the waveguides, using optical lithography and a lift-off process. We then patterned the ZnO layer using a wet-etch in dilute HCl. Hereupon, a 350 nm thick SiO$_2$ layer was deposited by PECVD. To expose the ZnO layer and the metal contacts, we used an electron-beam lithography system (Raith Voyager) to provide the required overlay accuracy, followed by RIE in CF$_4$, SF$_6$, and H$_2$ chemistry. After the removal of the remaining resist mask and etch residue in O$_2$ plasma, we used dilute KOH to remove the Al$_2$O$_3$ etch-stop layer and expose the ZnO electron injection layer. We then locally deposited a ≈20 nm layer of CdSe/CdS QDs by spin-coating them from toluene, using a lift-off procedure. High-resolution SEM images (see Figure S13, Supporting Information) confirm, that this process leads to a dense and uniform layer of QDs on top of the SiN waveguides. During the following shadow-mask evaporation of the organic layers we rotated the sample holder, to obtain homogeneous layers. We used a combination of 70 nm TCTA, 500 nm NPB, and 30 nm HAT-CN (sublimed grade, Ossila) for an optimized band-alignment, hole transport and injection (see **Figure 3**f). The devices were finalized with a 300 nm evaporated aluminum p-contact layer. The SEM micrograph in Figure 2g shows a focused ion beam (FIB) cross-section of a finished device, with the annotated sketch next to it outlining the different
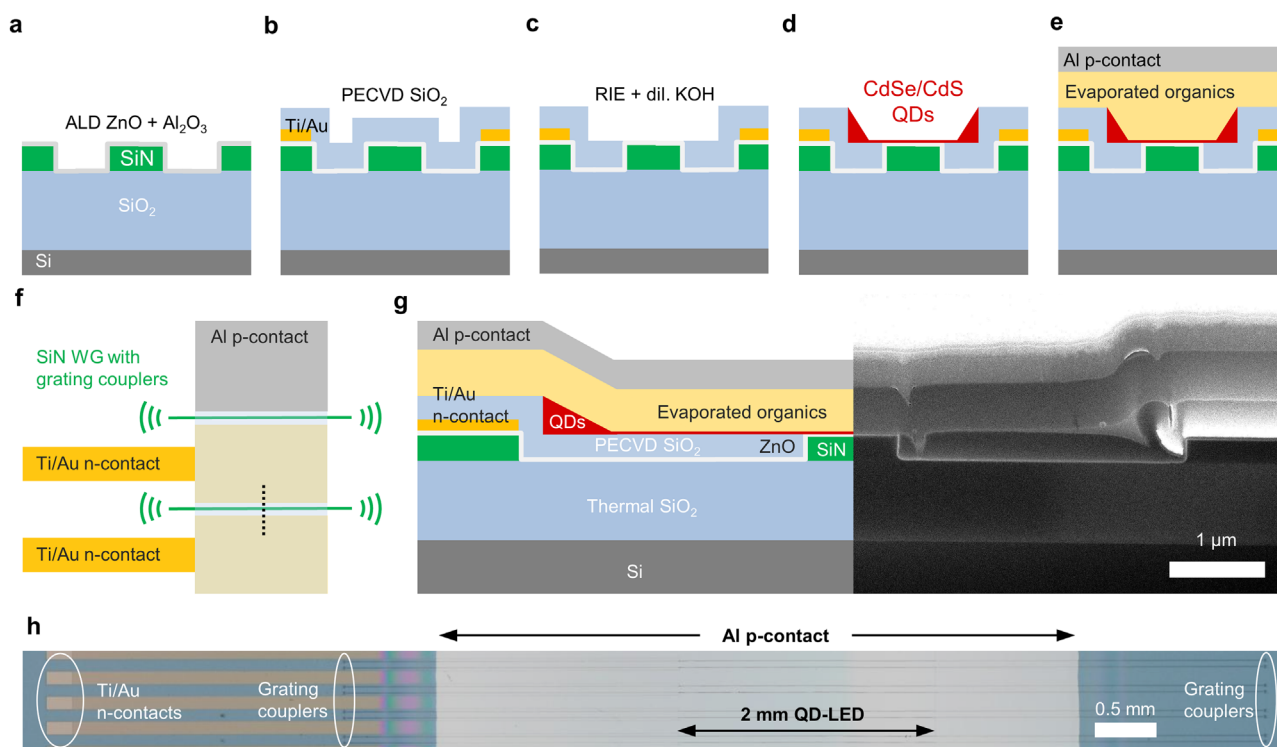
**ADVANCED
SCIENCE NEWS**

www.advancedsciencenews.com

LASER
& PHOTONICS
REVIEWS

www.lpr-journal.org

Figure 2. Processing steps to fabricate waveguide-coupled colloidal quantum dot LEDs and detectors. a) Atomic layer deposition (ALD) of the ZnO n-contact and an Al_2O_3 etch-stop layer on top of silicon nitride waveguides. b) Plasma-enhanced chemical vapor deposition (PECVD) of SiO_2 after patterning of metal contacts and ZnO. c) Reactive ion etch (RIE) of SiO_2 and KOH wet-etch of Al_2O_3. d) Local deposition of CdSe/CdS QDs using a lift-off process. e) Evaporation of organic hole transport layers and an aluminum p-contact. f) Schematic top-view of the device layout, with the dashed line indicating the location of the cross-section. (not to scale) g) High-resolution SEM micrograph of a focused ion beam (FIB) cross-section of a finished device. h) Optical microscope image of the sample showing eight devices.

layers. Additional details on the device fabrication can be found in Section S1, Supporting Information.

4. LED Characterization

The schematic top-view in Figure 2f shows that with our chip layout we were able to measure the waveguide transmission using grating couplers, while biasing the devices. For the devices presented here, we used one metal electrode to contact two waveguide-coupled QD-LEDs, increasing the number of devices (48 on one sample). Finite element simulations (Comsol Multiphysics) show, that this does not introduce any significant asymmetry of the electric fields (see Section S13, Supporting Information). To characterize the performance of the devices as waveguide-coupled LEDs, we used a source measurement unit (Keithley 2400) and DC probes to sweep the voltage and collected the output from the grating coupler with an optical fiber (SM780). Figure 3a shows the recorded current density for the device with the highest observed optical output power (device 1), reaching 47 A cm^{-2} at 100 V. However, for a different device on the same chip we recorded a current density as high as 100 A cm^{-2} at 120 V bias, just before device failure (see Section S7, Supporting Information). The output measured with an optical power meter (HP8153A) for a waveguide-coupled LED from a different chip (device 2) is displayed in Figure 3b, indicating an optical turn-on at a voltage of 3 V. This measurement is limited by the noise floor

of the optical power meter and we expect the actual value to be closer to the electrical turn-on at 2 V. Figure 3c shows the output spectrum of device 2 at 5 V bias. As the efficiency of the grating coupler has a strong spectral dependence, we cleaved the chip for this measurement and collected the emission from the end facet with a multimode fiber. There is a 15 nm red-shift of the spectrum, compared to the photoluminescence (PL) emission of the same CdSe/CdS QD sample in solution, while the full width at half maximum (FWHM) remains ≈35 nm. This is partly caused by short-range energy transfer from smaller to larger QDs, occurring in thin films.[20] Second, due to our device design, there is additional self-absorption of light propagating along the waveguide (see **Figure 4**a), limiting the output power of the LED (see Equation (2)) and further shifting the electroluminescence (EL) emission peak. Measuring with the grating coupler, we moreover observed a 2 nm red-shift of the peak emission wavelength for device 1, when increasing the bias voltage from 40 to 80 V (see Section S8, Supporting Information). We attribute this shift to the quantum confined Stark effect (QCSE),[21] in addition to a temperature increase of the active material,[22] due to the large bias voltage and current density.

Using a separate measurement of the grating coupler transmission spectrum (see Section S3, Supporting Information), we calculated an insertion loss of 13 dB, taking into account the QD emission spectrum. This allowed us to estimate the optical power in the silicon nitride waveguide. In addition, next to the 1 μm
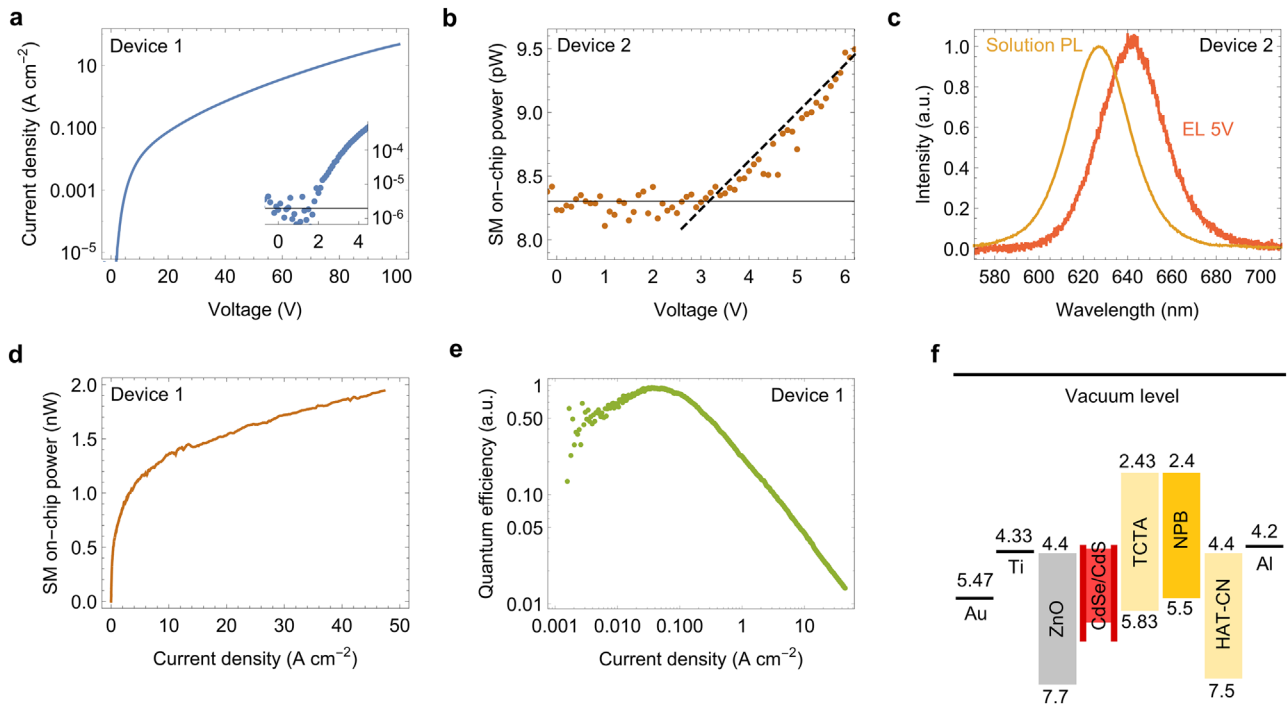
Figure 3. Characterization of the waveguide-coupled LED performance. a) Current density measured for the best-performing device. b) Optical turn-on measured on a second device. c) Electroluminescence output spectrum measured on a cleaved sample, compared to the solution PL of the CdSe/CdS QDs. d) Measured on-chip optical power in a single-mode waveguide and e) normalized quantum efficiency as a function of the current density. f) Band-alignment of the different layers in the device.
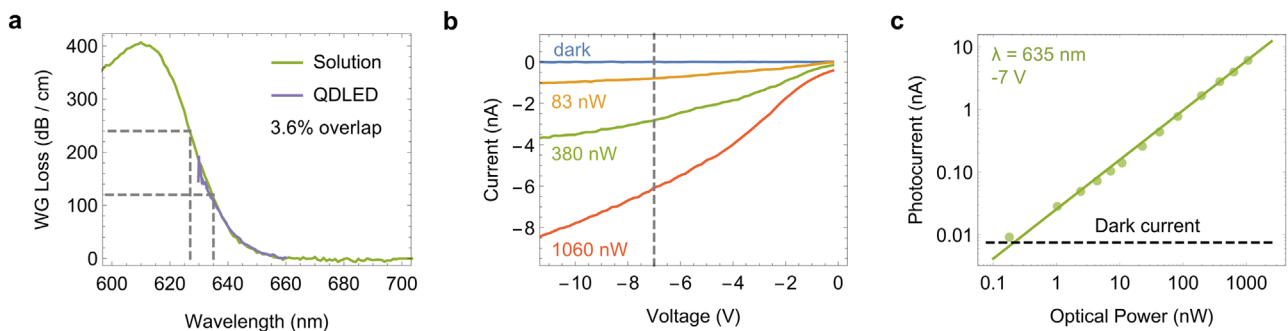

Figure 4. Detector performance of the wavguide-coupled QD LED devices. a) Absorption spectrum measured using grating couplers, compared to values calculated from a measurement of the CdSe/CdS QDs in solution. b) Current measured for different optical input powers of an external LED ($\lambda = 635$ nm) for a 500 µm long device. c) Photocurrent after subtraction of the dark current, for a reverse bias of 7 V and different optical input powers.

wide and 2 mm long QD-LED section, the silicon nitride photonic chips include 400 µm long single-mode filter sections, with 450 nm wide waveguides. This ensures, that the optical power collected through the grating coupler is from the fundamental TE mode only. Figure 3d shows the on-chip power in a single-mode waveguide, with a maximum of $P = 1.95$ nW optical power for a current density of 47 A cm^{-2}, for the 2 mm long device. We used this power to calculate the quantum efficiency ϕ of the QD-LED. Figure 3e shows the normalized quantum efficiency, with a maximum for a current density of 0.04 A cm^{-2} and a distinct roll-off behavior for higher current densities. A similar effect has been reported for many colloidal QD-LED devices in literature and is believed to originate from imperfect charge balance. It has been

shown, that adjusting the barrier for electron injection into the dots, can help to overcome this issue.[23,24] We calculated a maximum external quantum efficiency of $\phi_{ext} = 0.08\%$ for the device, according to

$$\phi_{ext} = \frac{P \lambda e}{I h c} \tag{1}$$

where e is the elementary charge, h the Planck constant, c the speed of light, I the device current, and the wavelength $\lambda = 642$ nm of the EL emission peak. The external quantum efficiency of our LEDs is low, compared to values reported for vertically emitting devices.[16] This is mainly due to the low average

coupling efficiency β_{avg} to the fundamental TE mode. In addition, next to the short-range energy-transfer reducing the PL quantum yield in thin films,[20] self-absorption is also a major loss mechanism in our waveguide-coupled devices. Neglecting the unlikely re-emission into the waveguide mode after an absorption event, the output power of a LED with length l can be modeled as

$$P(l) = p \int_0^l e^{-\alpha x} \, dx \qquad (2)$$

where the constant p is the coupled power per unit length and α is the self-absorption coefficient. Therefore, the fraction of power reaching the output is

$$\gamma = \frac{1 - e^{-\alpha l}}{\alpha l} \qquad (3)$$

The coefficient α can be extracted from the QD absorption in Figure 4a. For the PL emission peak at $\lambda = 627$ nm we obtained $\alpha = 5.5$ mm^{-1}. We then calculated the internal quantum efficiency for the 2 mm long devices according to

$$\phi_{int} = \frac{\phi_{ext}}{\beta_{avg}\gamma} \qquad (4)$$

obtaining a maximum of $\phi_{int} = 11\%$, for $\beta_{avg} = 0.8\%$ extracted from the simulation results in Figure 1b. Comparing this to a PL quantum yield of 75% for the CdSe/CdS QD sample in solution, there is still room for improvement in the device processing and the band alignment of the different layers shown in Figure 3f.

In literature, a saturation of the 1S-transition in colloidal QDs has been reported for a current density of 3.4 A cm^{-2}, corresponding to an average exciton density of $\langle N \rangle = 1.4$, which in turn limits the output-power of QD-LEDs.[9] For our devices, we used smaller CdSe/CdS QDs optimized for a high material gain.[17] With these QDs, a gain of $g_{i,th} = 880$ cm^{-1}, necessary to compensate the passive waveguide losses of 12 dB cm^{-1}, can be reached for $\langle N \rangle_{th} = 2$, using femto-second pulsed excitation.[17] Taking into account the different QD size and layer thickness in the work of Lim et al.,[9] we estimate a threshold current density of $j_{th} \approx 60$ A cm^{-2} for our devices (see Section S9, Supporting Information). However, the QD-LED output-power in Figure 3d already starts to saturate for a current density around 2 A cm^{-2}. Hence, we reason that a different effect causes the largest part of the observed saturation. From transient absorption experiments on the same QD sample in solution (see Section S10, Supporting Information), we know gain should first appear around a wavelength of 650 nm. Therefore, we monitored the waveguide transmission with an external CW laser ($\lambda = 650$ nm). But instead of the expected transparency, we observed an excess loss with increasing forward bias (see Figure S10, Supporting Information). We suspect, that this excess loss is partly caused by free carrier absorption in the ZnO layer and the aforementioned spectral shift at high bias voltages affecting the QD absorption, due to the QCSE and heating of the active material. From Figure S7, Supporting Information, we extracted a 2 nm red-shift of the EL emission, upon increasing the forward bias from 40 to 80 V. For a wavelength of 650 nm, a corresponding 2 nm red-shift of the QD absorption spectrum in Figure 4a should result in an additional loss of 7 dB cm^{-1}. Comparing this

to a loss of 17 dB cm^{-1} extracted from Figure S10, Supporting Information, for a corresponding voltage increase, Stark shift and heating account for less than half of the measured excess loss. Besides, a large fraction of the original transmission can only be recovered after keeping the device at a moderate reverse bias for several minutes. Hence we hypothesize, that trapped charges in the ZnO n-contact and the QD layer might be involved as well.

5. Detector Characterization

The same devices can also be operated as waveguide-coupled photo-detectors, using a moderate reverse bias. To characterize the detector performance, we first measured the transmission spectrum using the grating couplers (see Section S3, Supporting Information). The material absorption of CdSe and CdS nanoparticles for a wavelength of 350 nm reported in literature, was used to calculate the absorption of the core/shell particles with an effective medium approach.[25,26] In Figure 4a we compare the detector absorption to values calculated from the absorption spectrum of the CdSe/CdS QDs in solution. Assuming a QD fill-factor of 50% and a mode overlap of 3.6%, corresponding to a QD layer thickness of 22 nm, we observe a good agreement with the waveguide-based measurement. For the detector characterization we used an external LED ($\lambda = 635$ nm) and estimated the power coupled into a single-mode waveguide from the transmission spectrum of a device without quantum dots (see Section S12, Supporting Information). Figure 4b compares the device current measured for different optical input powers to the dark current for a 500 μm long device. We then used the photocurrent at a reverse bias of 7 V, subtracted the dark current of 1.5 μA cm^{-2} and fitted the detector response in Figure 4c with

$$I(P) = a \, P^b \qquad (5)$$

giving $a = 0.025$ A W^{-1} and $b = 0.8$. A possible explanation of the observed non-linear detector response might be the creation of trions and bi-excitons for larger input powers, for which we expect the charge extraction to become less efficient. However, the maximum power of 1 μW, corresponding to a power density of 0.18 kW cm^{-2} in the QD layer, only causes an excitation level of $\langle N \rangle \approx 0.01$, assuming a 15 ns average lifetime for the QD sample.[17] Therefore, we reason that the non-linearity is caused by a different effect, related to the observation that the photocurrent is not saturated for a reverse bias of 7 V, as can be seen in Figure 4b. We suspect that this is due to the low electrical conductivity of the oleic acid ligands covering the QDs, which ensure a high PL quantum yield. For a wavelength of 635 nm, it can be extracted from Figure 4a, that 75% of the incident power is absorbed in the detector, which limits the attainable detector quantum efficiency. Without any optimization of the devices, we extracted a detector quantum efficiency of 6% for an input power of 0.3 nW. With further improvements of the band alignment and device processing we expect to reach a detector performance, which is on par with planar devices reported in literature.[27]

6. Conclusion

In summary, we have demonstrated waveguide-coupled colloidal quantum dot devices, which can be operated as detectors and

LEDs. We anticipate that these devices can find applications in chip-based absorption spectroscopy, as they can be post-processed on foundry-fabricated waveguide platforms, at a low cost. For the LEDs we report a record current density of up to 100 A cm^{-2} and a maximum on-chip power of almost 2 nW, corresponding to a power density of 1.5 W cm^{-2} in a single-mode waveguide. The detectors have a low dark current of 1.5 μA cm^{-2} at a reverse bias of 7 V, but show a non-linear photocurrent response. We believe, that with further progress in the process development, we can improve the internal quantum efficiency of both types of devices to reach the values reported in literature for planar designs.[16,27] The LED output power of 2 nW is mainly limited by the poor average coupling efficiency $\beta_{avg} = 0.8\%$, governing the process of spontaneous emission. However, for lasers and amplifiers the small mode overlap in our devices is less of a problem. With the reported current densities stimulated emission is within reach,[9] potentially enabling output powers in the μW range and a corresponding improvement of the external quantum efficiency. While the devices are currently still limited by adverse effects hampering the observation of optical transparency, we believe that our approach solves a key challenge in building an electrically pumped laser using colloidal QDs. In addition to inherent current-focusing built into our devices, the passive silicon nitride waveguide makes it possible to decouple the optical mode profile from the thickness of the QD layer. In combination with the low-loss n-contact layer, also thin QD layers, which can be inverted using an electrical bias,[9] are expected to provide sufficient gain for lasing to occur.

Supporting Information

Supporting Information is available from the Wiley Online Library or from the author.

Acknowledgements

Conflict of Interest

The authors declare no conflict of interest.

Keywords

[1] C. Dang, J. Lee, C. Breen, J. S. Steckel, S. Coe-Sullivan, A. Nurmikko, *Nat. Nanotechnol.* **2012**, *7*, 335.

[2] C. Dang, J. Lee, K. Roh, H. Kim, S. Ahn, H. Jeon, C. Breen, J. S. Steckel, S. Coe-Sullivan, A. Nurmikko, *Appl. Phys. Lett.* **2013**, *103*, 171104.

[3] M. M. Adachi, F. Fan, D. P. Sellan, S. Hoogland, O. Voznyy, A. J. Houtepen, K. D. Parrish, P. Kanjanaboos, J. A. Malen, E. H. Sargent, *Nat. Commun.* **2015**, *6*, 8694.

[4] W. Xie, T. Stöferle, G. Rainò, T. Aubert, S. Bisschop, Y. Zhu, R. F. Mahrt, P. Geiregat, E. Brainis, Z. Hens, D. Van Thourhout, *Adv. Mater.* **2017**, *29*, 1604866.

[5] Y. Zhu, W. Xie, S. Bisschop, T. Aubert, E. Brainis, P. Geiregat, Z. Hens, D. Van Thourhout, *ACS Photonics* **2017**, *4*, 2446.

[6] F. Fan, O. Voznyy, R. P. Sabatini, K. T. Bicanic, M. M. Adachi, J. R. McBride, K. R. Reid, Y.-S. Park, X. Li, A. Jain, R. Quintero-Bermudez, M. Saravanapavanantham, M. Liu, M. Korkusinski, P. Hawrylak, V. I. Klimov, S. J. Rosenthal, S. Hoogland, E. H. Sargent, *Nature* **2017**, *544*, 75.

[7] Z. Yang, M. Pelton, I. Fedin, D. V. Talapin, E. Waks, *Nat. Commun.* **2017**, *8*, 143.

[8] Y. Shirasaki, G. J. Supran, M. G. Bawendi, V. Bulović, *Nat. Photonics* **2013**, *7*, 13.

[9] J. Lim, Y.-S. Park, V. I. Klimov, *Nat. Mater.* **2018**, *17*, 42.

[10] J. Roh, Y.-S. Park, J. Lim, V. I. Klimov, *Nat. Commun.* **2020**, *11*, 271.

[11] A. Z. Subramanian, E. Ryckeboer, A. Dhakal, F. Peyskens, A. Malik, B. Kuyken, H. Zhao, S. Pathak, A. Ruocco, A. De Groote, P. Wuytens, D. Martens, F. Leo, W. Xie, U. D. Dave, M. Muneeb, P. Van Dorpe, J. Van Campenhout, W. Bogaerts, P. Bienstman, N. Le Thomas, D. Van Thourhout, Z. Hens, G. Roelkens, R. Baets, *Photonics Res.* **2015**, *3*, B47.

[12] X. Ji, F. A. S. Barbosa, S. P. Roberts, A. Dutt, J. Cardenas, Y. Okawachi, A. Bryant, A. L. Gaeta, M. Lipson, *Optica* **2017**, *4*, 619.

[13] K. Alexander, J. P. George, J. Verbist, K. Neyts, B. Kuyken, D. Van Thourhout, J. Beeckman, *Nat. Commun.* **2018**, *9*, 3444.

[14] C. Op de Beeck, B. Haq, L. Elsinger, A. Gocalinska, E. Pelucchi, B. Corbett, G. Roelkens, B. Kuyken, *Optica* **2020**, *7*, 386.

[15] C. Xiang, W. Jin, J. Guo, J. D. Peters, M. J. Kennedy, J. Selvidge, P. A. Morton, J. E. Bowers, *Optica* **2020**, *7*, 20.

[16] B. S. Mashford, M. Stevenson, Z. Popovic, C. Hamilton, Z. Zhou, C. Breen, J. Steckel, V. Bulovic, M. Bawendi, S. Coe-Sullivan, P. T. Kazlas, *Nat. Photonics* **2013**, *7*, 407.

[17] S. Bisschop, P. Geiregat, T. Aubert, Z. Hens, *ACS Nano* **2018**, *12*, 9011.

[18] Y. Y. Ussembayev, Z. Hens, K. Neyts, *ACS Photonics* **2019**, *6*, 1146.

[19] A. Rahim, J. Goyvaerts, B. Szelag, J.-M. Fedeli, P. Absil, T. Aalto, M. Harjanne, C. Littlejohns, G. Reed, G. Winzer, S. Lischke, L. Zimmermann, D. Knoll, D. Geuzebroek, A. Leinse, M. Geiselmann, M. Zervas, H. Jans, A. Stassen, C. Dominguez, P. Munoz, D. Domenech, A. L. Giesecke, M. C. Lemme, R. Baets, *IEEE J. Sel. Top. Quantum Electron.* **2019**, *25*, 1.

[20] N. Kholmicheva, P. Moroz, H. Eckard, G. Jensen, M. Zamkov, *ACS Energy Lett.* **2017**, *2*, 154.

[21] S. A. Empedocles, *Science* **1997**, *278*, 2114.

[22] D. Pugh-Thomas, B. M. Walsh, M. C. Gupta, *Nanotechnology* **2011**, *22*, 185503.

[23] Z. Zhang, Y. Ye, C. Pu, Y. Deng, X. Dai, X. Chen, D. Chen, X. Zheng, Y. Gao, W. Fang, X. Peng, Y. Jin, *Adv. Mater.* **2018**, *30*, 1801387.

[24] J. Lim, Y.-S. Park, K. Wu, H. J. Yun, V. I. Klimov, *Nano Lett.* **2018**, *18*, 6645.

[25] Z. Hens, I. Moreels, *J. Mat. Chem.* **2012**, *22*, 10406.

[26] Y. Justo, P. Geiregat, K. V. Hoecke, F. Vanhaecke, C. De Mello Donega, Z. Hens, *J. Phys. Chem. C* **2013**, *117*, 20171.

[27] P. Malinowski, E. Georgitzikis, J. Maes, I. Vamvaka, F. Frazzica, J. Van Olmen, P. De Moor, P. Heremans, Z. Hens, D. Cheyns, *Sensors* **2017**, *17*, 2867.